Influence of argon, helium, and their mixtures on the powder bed fusion of an Al–Cu–Li–Ti alloy using a laser beam: Evaporation, microstructure, and mechanical properties

Siegfried Baehr [a],[*], Graham Matheson [b],[c], Thomas Ammann [d], Peter Mayr [b], Michael F. Zaeh [a]

[a] Technical University of Munich, TUM School of Engineering and Design, Department of Mechanical Engineering, Institute for Machine Tools and Industrial Management, Boltzmannstrasse 15, 85748, Garching, Germany
[b] Technical University of Munich, TUM School of Engineering and Design, Department of Materials Engineering, Chair of Materials Engineering of Additive Manufacturing, Freisinger Landstrasse 52, 85748, Garching, Germany
[c] Oerlikon AM Europe GmbH, Freisinger Landtrasse 52, 85748 Garching, Germany
[d] Linde GmbH, Carl-von-Linde-Strasse 25, 85716, Unterschleissheim, Germany

ARTICLE INFO

ABSTRACT

The role of the inert processing gas during the powder bed fusion of metals using a laser beam (PBF-LB/M) is to prevent oxidation and remove process by-products, such as metal vapor and spatter particles. The present study aims to unveil additional impacts of using argon (Ar), helium (He), and two mixtures thereof as the processing gas on the material properties of a high-strength Al–Cu–Li–Ti alloy fabricated by PBF-LB/M. The part density, microstructure, static tensile properties, and volatile element evaporation were characterized as functions of the processing gas. Decreased porosity levels and increased melt penetration depths were found across a range of processing parameters when increasing the fraction of He in Ar indicating a more stable process and melt pool dynamics. A trend towards increasing yield and ultimate tensile strength was also observed and was attributed to a slightly refined grain size when processing under He-containing gases. The process gas had no significant influence on the evaporation of alloying constituents in the material. Overall, several advantages of using He-containing process gases over pure Ar in PBF-LB/M are demonstrated and discussed.

1. Introduction and state of research

The powder bed fusion of metals using a laser beam (PBF-LB/M) is an additive manufacturing (AM) process that enables a tool-free fabrication of geometrically complex parts with integrated functionalities in a near-net shape and is one of the most industrially relevant AM processes. However, the process still faces various challenges, such as a relatively low reproducibility of the part properties. To overcome current issues, a holistic understanding of the relevant interactions during PBF-LB/M is crucial.

The process gas plays a significant role in realizing a stable and reproducible process, but is less frequently studied than the standard process parameters, such as the laser power or the scanning speed. Before the laser exposure of the powder bed, the build chamber is flooded with gas, typically argon (Ar) or nitrogen (N_2), to lower the level of remaining oxygen in the atmosphere to values under a defined

threshold, typically 0.2 or 0.1 vol.-% (Gebhardt, 2016). During the layer-by-layer build-up, a continuous gas flow is directed over the build platform to remove by-products (e.g., spatter and fumes) from the laser-powder interaction zone. In addition to controlling the gas flow velocity, the choice of the gas type can further contribute to a more stable process.

This can be of particular interest when it comes to processing novel alloys by PBF-LB/M, such as high-strength aluminum (Al) alloys. These alloys often suffer from various cracking phenomena during PBF-LB/M processing. So maintaining a stable process is, therefore, a prerequisite to properly handle those alloys.

1.1. Process gas influence

The studies available to date mainly focused on the influence of the gas flow velocity (Baehr et al., 2023; Ladewig et al., 2016; Reijonen

---

* Corresponding author.
E-mail address: siegfried.baehr@iwb.tum.de (S. Baehr).

et al., 2020) as well as the gas type (Amano et al., 2021; Baehr et al., 2022; Ch et al., 2019; Pauzon et al., 2021; Traore et al., 2021; Wimmer et al., 2018) on the PBF-LB/M process. The research on the former topic unveiled the significance of a sufficient gas flow velocity for the removal of spatter and fumes (Ladewig et al., 2016; Reijonen et al., 2020). The highest possible gas flow velocity should, therefore, be aimed for. However, in order to protect feedstock particles on the surface of the powder bed from being blown away, the gas type specific particle pickup velocity needs to be considered (Baehr et al., 2023). It was found that higher flow velocities can be applied with helium (He) compared to Ar due to its higher particle pickup velocity (Baehr et al., 2023). Various further experimental studies investigated the influence of a varying gas type on the PBF-LB/M process. With Ar as the reference gas, the main gases compared were N_2 (Ch et al., 2019; Pauzon et al., 2019; Wimmer et al., 2018), He (Amano et al., 2021; Pauzon et al., 2021; Wimmer et al., 2018; Wirth et al.), and their mixtures. Overall, N_2 was found to lead to no significant improvements or deteriorations of the process. In studies with the materials AlSi10Mg (Ch et al., 2019) and 316 L (Pauzon et al., 2019), comparable surface roughness values, porosities, and static tensile properties of parts were found for processing under N_2 or Ar. No differences were found in the number of created spatter between Ar and N_2 (Wimmer et al., 2018). In contrast, the use of He showed a greater impact on the PBF-LB/M process. For the material Ti–6Al–4V, refined microstructures were found under He compared to Ar, resulting in slightly higher static tensile properties of approximately 4.5 % for the tensile strength (Amano et al., 2021). This finding was attributed to the faster cooling rates while processing under He (Amano et al., 2021; Pauzon et al., 2021). Also, the advantages of He were demonstrated with fewer incandescent spatter being created and, thus, a more stable PBF-LB/M process (Baehr et al., 2022; Pauzon et al., 2021; Traore et al., 2021). It was shown that this effect is material-independent and is based on the approximately ten times as high thermal conductivity and approximately nine times as high specific heat capacity of He compared to Ar (Baehr et al., 2022). The more stable process also led to a lower total spatter mass leaving the melt pool and landing in the powder bed, decreasing the probability of defects (Baehr et al., 2023; Wimmer et al., 2018).

1.2. High-strength aluminum alloys

Mechanical strength is normally increased in Al alloys by three basic mechanisms, namely: solid solution strengthening, grain refinement, and precipitation of intermetallic phases after heat treatment. Achieving a room temperature yield strength in excess of 400 MPa typically requires additions of alloying elements in amounts that hinder compatibility with PBF-LB/M processing. Still, high-strength Al alloys that can be processed by PBF-LB/M are demanded by various industries, such as the aerospace sector (Dixit and Liu, 2022; Rometsch et al., 2022). However, the rapid heating and cooling rates of the melt pool inherent to the PBF-LB/M process can lead to cracks in high-strength Al parts. These cracks can originate from a variety of cracking mechanisms during the rapid solidification and form primarily along elongated grain boundaries (Kusoglu et al., 2020). Various studies have tackled this issue by two common approaches: adapting the process parameters (Hu et al., 2020; Stopyra et al., 2020) or adjusting the alloy composition (Aversa et al., 2019; Mair et al., 2021; Mertens et al., 2020; Schimbäck et al., 2022). The processing approach typically requires a strong decrease of the scanning speed to reduce the thermal gradient (Hu et al., 2020). This approach, however, results in industrially impractical process conditions, because build-up rates are too low. The grain refinement approach has been shown in various studies to be a promising way to make those alloys processable. The alloying elements titanium (Ti), scandium (Sc), and zirconium (Zr) were extensively applied to Al alloys from the 2000 (copper (Cu) as the main alloying element), 6000, and 7000 series, whereby the grain refinement through the creation of Al_3X (X = Ti, Sc, or Zr) led to the suppression of cracks via heterogenous nucleation of

fine equiaxed Al grains (Aversa et al., 2018; Mertens et al., 2020; Schimbäck et al., 2022). Other approaches added reinforcing particulates (e.g., Ti diboride or other ceramics) to mitigate cracking phenomena (Mair et al., 2021; Varmus et al., 2023). Another issue that needs to be considered during the processing of these Al alloys is the evaporation of volatile elements. In this study, volatile elements are defined as metallic alloying additions that have a pure elemental boiling temperature lower than the boiling temperature of Al. Magnesium (Mg), zinc (Zn), and lithium (Li) are of particular interest in this regard, as their evaporation reduces their strengthening effects and can lead to the creation of gas pores during PBF-LB/M processing (Rometsch et al., 2022).

1.3. Summary and scope of the work

On the one hand, the presented state of research has shown that applying gases other than Ar or N_2 can lead to an increased PBF-LB/M process capability. On the other hand, the processing of high-strength Al alloys still poses challenges regarding cracking and volatile element evaporation. Therefore, this study aims to unveil the influence of Ar, He, and their mixtures on the processing of a 2000 series Al–Cu–Li–Ti alloy. Test specimens were fabricated under pure Ar and pure He processing gas and mixtures thereof to study their influence on the part density, microstructure, chemical composition, and static mechanical properties of the Al–Cu–Li–Ti alloy system. The following research questions were addressed regarding the PBF-LB/M process:

- To what extent does the use of He or Ar–He mixtures influence the PBF-LB/M process stability?
- How does the use of He or Ar–He mixtures influence the microstructure of high-strength Al parts?
- Can increased mechanical properties of high-strength Al parts be achieved using He or Ar–He mixtures?

2. Materials and methods

2.1. Fabrication of specimens

All specimens in this study were fabricated on a PBF-LB/M machine (AconityMINI, Aconity3D GmbH, Germany) with a maximum laser power of 500 W and a laser spot diameter of 80 μm. Two different build job layouts served for the experiments as outlined in Fig. 1. The gases Ar, He, and their mixtures of 70 vol.-% Ar + 30 vol.-% He (ArHe30) and 30 vol.-% Ar + 70 vol.-% He (ArHe70), provided as pre-mixed gases (Linde GmbH, Germany), were used in this study. Each build job layout was printed with each of the four gases. Prior to the build jobs, the oxygen content in the build chamber was lowered to below 0.05 vol.-% (500 ppm). The oxygen level was monitored during processing with the lambda sensor built into the PBF-LB/M machine (ZR5-1.1 A, ZIROX GmbH, Germany). The gas flow velocity was set to 2 m/s for all gases.

For the initial parameter study, the layout depicted in Fig. 1a was used. A full-factorial experimental plan was applied. The three parameters varied in three levels were the laser power P (200, 250, and 300 W), the scanning speed v (600, 800, and 1000 mm/s), and the hatch distance h (0.08, 0.09, and 0.10 mm). The selection of the parameters and their levels was based on the literature (Mair et al., 2021). The layer thickness t was kept constant at 0.03 mm. A bi-directional scan pattern was applied with a 67° rotation angle between the layers. No preheating was used. For the comparison of the results, the volumetric energy density (VED), a parameter combining P, v, h, and t, was calculated as follows:

$$\text{VED} = \frac{P}{v \bullet h \bullet t}.$$

The value of VED ranged from 66.7 to 208.3 J/mm³. In total, the layout consisted of 27 cuboids with a dimension of $10 \times 10 \times 13$ mm³. In
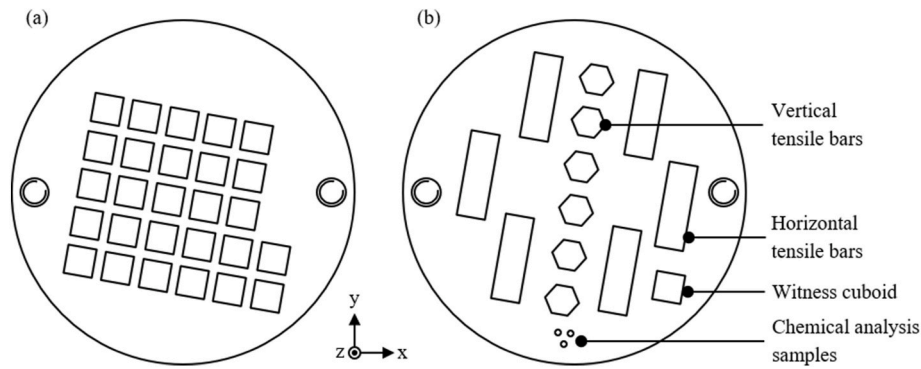
Fig. 1. Schematic build job layouts (not to scale): (a) parameter study, (b) mechanical properties study; negative x: gas flow direction, y: recoating direction, z: building direction.

the second part of the study, the layout for the mechanical tests shown in Fig. 1b was applied. For these build jobs, *P* was set to 200 W, *v* to 800 mm/s, and *h* to 0.08 mm, as these parameters led to high relative part densities above 99.7 % for all gases. The layout consisted of six horizontal and six vertical tensile bars, one witness cuboid for the density ($10 \times 10 \times 13$ mm^3), and three cylinders for chemical analyses (diameter: 3 mm, height: 13 mm). The bars for tensile testing were machined from specimens fabricated with a hexagonal cross-section with an edge length of 6 mm, and a total length of 65 mm. In a repetition job, six horizontal tensile bars were printed. In total, 18 tensile bars were printed for each processing gas. To qualitatively observe the spatter formation during processing with different gases, a digital camera (PowerShot SX50 HS, Canon Inc., Japan) was used.

2.2. Powder feedstock material and chemical analysis

A gas-atomized, pre-alloyed Al–Cu–Li–Ti powder was used as feedstock material (NANOVAL GmbH, Germany). The powder was sieved by the manufacturer to separate a nominal particle size fraction between 20 and 63 μm for PBF-LB/M processing. The particle size distribution (PSD) of the feedstock powder was analyzed via the laser diffraction method (Mastersizer 3000, Malvern Panalytical, UK). Three replicates were measured, each consisting of a volume of approximately 50 mm^3. The chemical compositions of the powder and of the printed specimens after the process were measured by inductively coupled plasma optical emission spectrometry (ICP-OES) (5110 ICP-OES, Agilent Technologies, USA) for metallic elements and by inert gas fusion (IGF) (ONH 836, LECO, USA) for oxygen (O) and hydrogen (H).

2.3. Density and metallography

After fabrication, the absolute density was measured with the Archimedes principle using a precision scale (PET 600-3 M, KERN & SOHN GmbH, Germany). Ethanol served as the liquid for the measurements. The temperature of the liquid was constantly monitored and, if needed, adjusted for the density calculations. Each cuboid was measured three times. The surfaces of the cuboids were polished with a 220# polishing paper prior to the measurements to avoid bubble creation. After the absolute density measurements, the cuboids were halved and cold-embedded using a resin (EpoFix Resin, Struers GmbH, Germany) and a hardener (EpoFix Hardener, Struers GmbH, Germany) in a ratio of 25:3. Subsequently, the cuboids were ground and finally polished to 0.05 μm using a silica suspension (OP–S NonDry, Struers GmbH, Germany). The full grinding and polishing routine is given in the Appendix A. An exemplary result of this procedure is shown in Fig. 2a. The relative density was then determined on micrographs an optical microscope (VHX-6000, Keyence Deutschland GmbH, Germany) using a threshold-based image processing approach.

For the determination of the penetration depth, the cuboids were etched in the next step. Polished cuboids were immersed into Keller-Wilcox etchant consisting of HNO$_3$, HCl, and HF in water (Bernd Kraft GmbH, Germany) for a duration of 10 s. The penetration depth was then measured by optical microscopy as shown in Fig. 2b. The average value of ten measurements per cuboid was considered.

2.4. Microstructure analysis

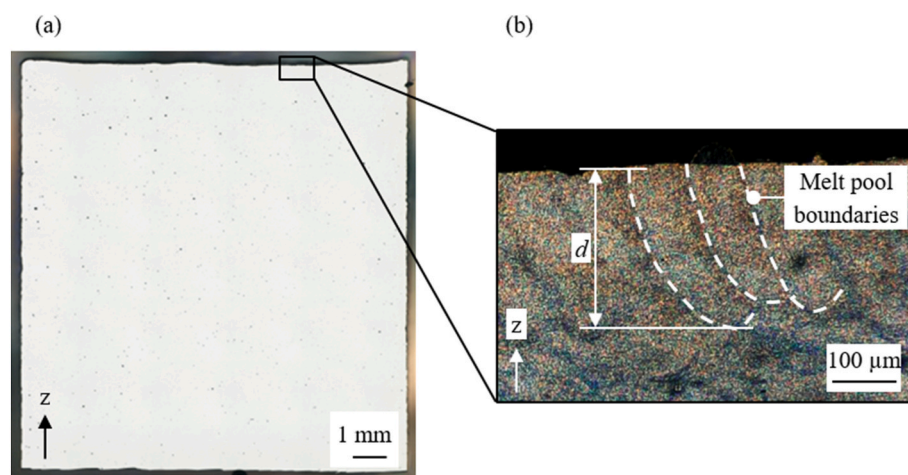The microstructure of the solid material and the powder particles

Fig. 2. (a) Optical micrograph of a cross-section of a cuboid after polishing, (b) principle of the penetration depth measurements; z: building direction.

was investigated in the second part of the study using a field emission scanning electron microscope (SEM) (Merlin Gemini II 6006, Zeiss AG, Germany). Secondary and backscatter electron micrographs were acquired with an acceleration voltage of 10 kV and a probe current of 2.5 nA. The distribution of the elements was mapped with an energy-dispersive X-ray spectroscopy (EDS) detector (X-MaxN, Oxford Instruments, UK) and the grain size was quantified with an electron backscatter diffraction (EBSD) detector (Nordlys Nano, Oxford Instruments, UK). The EBSD measurements were conducted at 1000x magnification with a constant scanning area of 112 x 84 μm^2 for each specimen with a 270 nm step size, ensuring a minimum of 4000 grains for representative grain size statistics. The analysis of the EBSD data was carried out via software processing (Matlab MTEX toolbox, MathWorks, US).

2.5. Mechanical testing

Before testing according to the ASTM E8M standard, the as-fabricated hexagonal blanks were machined to the round tensile test specimen design 3 given in the standard. The tensile bars were tested without heat treatment. The tests were performed on a universal test machine (Z100 TN, ZwickRoell GmbH & Co. KG, Germany) at room temperature. The fracture surfaces were further investigated using an SEM (JSM-IT200 InTouchScope, JEOL GmbH, Germany). The secondary electron micrographs were captured with an acceleration voltage of 30 kV and working distances ranging from 10.4 to 14.2 mm.

3. Results

3.1. Powder characterization

The laser diffraction PSD measurements showed percentiles of $d_{10} = 18.1 \pm 0.1$ μm, $d_{50} = 31.9 \pm 0.1$ μm, and $d_{90} = 59.9 \pm 0.1$ μm. The chemical composition was determined according to Table 1. The SEM micrographs in Fig. 3 exposed the shape and microstructure of the powder. Fig. 3a shows that mainly spherical powder particles with some irregularly shaped agglomerates were present. The internal microstructure of the powder particles in Fig. 3b exhibited a Cu-rich cellular structure with Ti-rich intermetallic particles in the EDS investigation.

3.2. Qualitative process observation

Two frames from the process videos captured at the same point in time during processing are shown in Fig. 4. In the Ar process (see Fig. 4a), a higher number of incandescent spatter particles are observable compared to the He process. Interactions between the laser and spatter particles are also visible as marked in Fig. 4a. Here, a cooled-off spatter crosses the laser beam path, which leads to a re-melting and, thus, a visible light track in the frame. In the He process shown in Fig. 4b, less process lighting is apparent with no visible laser-spatter interactions.

3.3. Porosity and penetration depth

The results from the density measurements are shown in Fig. 5 over the VED, with Fig. 5a and b showing the relative and absolute densities, respectively. The grey triangles belong to the results for Ar and the blue circles belong to the results for He. Only for the absolute density measurements, a standard deviation was calculated. The results for the gas mixtures ArHe30 and ArHe70 are shown in the Appendix B.

For both processing gases, a qualitative trend towards lower densities in the as-fabricated cuboids with an increasing VED can be observed. The Ar results show a higher standard deviation over all samples. The absolute densities of specimens processed with Ar spread in a range from 2.61 to 2.66 g/cm^3 (relative densities: 97.6–99.8 %). For He processing, the results range from 2.63 to 2.66 g/cm^3 (relative densities: 98.6–99.8 %). In all gases, only spherical pores were found.

To determine the significant parameters on the density, an analysis of variance (ANOVA) was performed. As independent variables, P, v, h, and the gas type were selected. The relative density was chosen as the dependent variable. The analysis comprised interactions up to the 2nd order. The results, which are summarized in the Appendix C, showed that only the laser power P, the gas type, and their interaction significantly influence the density (p values $<$ 0.05). Since the regression coefficient for P was negative, it could be stated that an increasing laser power led to a decreasing density. In contrast, an increasing density occurred with an increasing He content in the processing gas, since its regression coefficient was positive. Their interaction exhibited, that a higher laser power was needed with an increasing He content in the processing gas to achieve high densities.

Table 2 summarizes the results from the penetration depth measurements for all four processing gases ($P = 200$ W, $v = 800$ mm/s, $h = 0.08$ mm). The results indicate a trend towards higher penetration depths d with an increasing He content, increasing by approximately 10 % from Ar to He. The highest penetration depth of 207 μm was found in the ArHe30 sample.

3.4. Evaporation of elements

Table 3 shows the results of the chemical composition measurements by IGF and ICP-OES for the feedstock powder and solid samples fabricated under the four processing gases. A decrease in the mass fraction of the volatile elements Li, Mg, and Zn in the processed material as compared to powder could be observed. The alloying elements Cu and Ti had no measurable evaporation. For the elements O, H, Mg, and Zn, a higher evaporative loss under Ar processing compared to He processing was found. However, considering the measurement uncertainty, no significant difference between the gases could be definitively stated. The highest relative amount of evaporation from powder to processed material among the metallic constituents was found for Zn, where 27 % of the Zn in the alloy powder was lost from the final part due to the laser interaction.

3.5. Microstructure

The solid material under all process gases is free of hot-cracking in the as-built state due to the refined grain structure. The grain size distribution in the microstructure of the Ar and He processed samples gathered via EBSD is shown in Fig. 6a for various size classes. A shift towards finer grain sizes could be observed for the samples fabricated under He as compared to Ar. This is especially the case for the sub-2μm grain size classes in Fig. 6a. In the larger grain size classes, the Ar sample exposes a significantly higher number of grains compared to the He sample. Fig. 6b and c additionally depict SEM images of the cross sections of the parts manufactured under Ar and He. Like the powder particles themselves, the solidified as-printed alloy has alloying element (Cu, Zn, and Mg) enrichment along the fine grain boundaries and submicron Al$_3$Ti precipitates in the grain interiors. The results for the specimens processed using Ar–He gas mixtures lie in between the results for specimens processed with Ar or He and are summarized in Appendix
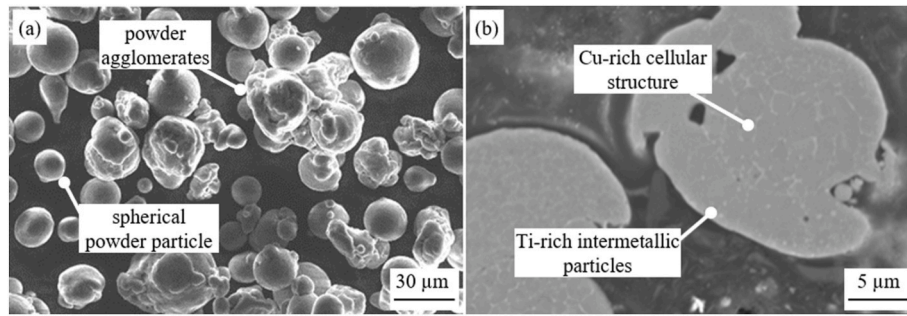
Table 1
Chemical composition of the aluminum alloy powder.

Element	Al	Cu	Li	Ti	Zn	Mg	O	N	H
Composition (m%)	Balance	2.7 ± 0.1	1.8 ± 0.1	1.3 ± 0.1	0.59 ± 0.04	0.27 ± 0.03	0.04 ± 0.01	0.006 ± 0.001	0.007 ± 0.001

Fig. 3. SEM micrographs of the aluminum powder: (a) overview, (b) detailed cross section.
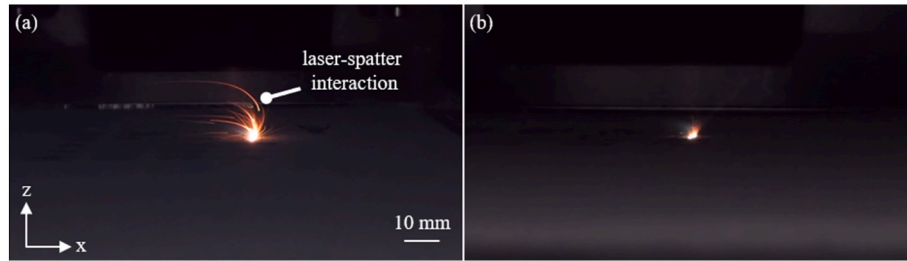

Fig. 4. Two frames from the videos captured at the same section from the (a) argon and (b) helium process; negative x: gas flow direction, z: building direction.
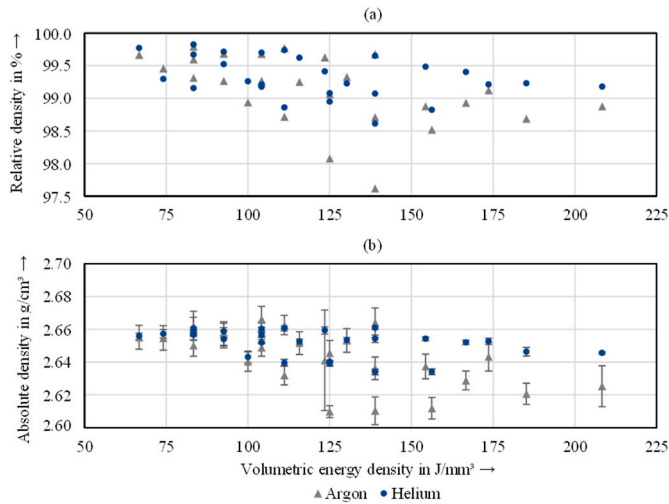

Fig. 5. Results from the density measurements in the samples processed under argon and helium; (a) relative density, (b) absolute density.

Table 2
Penetration depth measurements.

Processing Gas	Ar	ArHe30	ArHe70	He
Mean penetration depth d	179 µm	207 µm	189 µm	197 µm
Standard deviation	12 µm	7 µm	3 µm	10 µm

D. For completeness, the EBSD data for specimens processed with various gases are additionally shown in the Appendix E.

3.6. Static mechanical properties

The results from the static mechanical tests are summarized in Fig. 7a, showing the mean values over all samples processed with various gases. The yield strength R_{eH} shows no significant difference between Ar, ArHe30, and He processing. However, a significant peak for

Table 3
Results from the evaporation measurements by IGF and ICP-OES in mass percentage (m%); the processing gas for the analyzed specimens is indicated.

Analyzed elements	Powder	Ar	ArHe30	ArHe70	He
O in m% (error: $\pm$ 0.006)	0.040	0.021	0.026	0.023	0.023
H in m% (error: $\pm$ 0.001)	0.007	0.003	0.006	0.003	0.004
Cu in m% (error: $\pm$ 0.1)	2.7	2.7	2.7	2.7	2.7
Li in m% (error: $\pm$ 0.1)	1.8	1.7	1.7	1.7	1.7
Mg in m% (error: $\pm$ 0.03)	0.27	0.22	0.22	0.23	0.23
Zn in m% (error: $\pm$ 0.04)	0.59	0.43	0.44	0.44	0.45
Ti in m% (error: $\pm$ 0.1)	1.3	1.3	1.3	1.3	1.3

R_{eH} of 422 MPa was found for samples processed with the ArHe70 mixture. The tensile strength R_m reaches its maximum at 408 MPa with ArHe70 processing and similar values were found for Ar and He samples with 401 and 400 MPa, respectively. Considering the standard deviation, the elongation at break A shows no trend with mean values of 12.8 % (Ar processing) and 13.5 % (He processing). The associated fracture surfaces captured by SEM for Ar and He processing are shown in Fig. 7b and c. The He sample in Fig. 7c seems to have suffered from a more brittle fracture behavior than the Ar processed sample. In the Ar processed sample, a more ductile fracture behavior was found (see Fig. 7b). The fracture surfaces for ArHe30 and ArHe70 gas mixture processing are shown in the Appendix F. The trend towards apparently more brittle fracture behavior with an increasing He content is evident in these images.

4. Discussion

4.1. Process stability and part porosity

The differences in the process lighting shown in Fig. 4 coincide with results from the literature, where the creation of fewer incandescent spatters was linked to the higher cooling ability of He compared to Ar (Baehr et al., 2022; Pauzon et al., 2021). As this is a result of the thermal properties of the gas and, thus, is material-independent, the same influence was found in the processes in this study. Furthermore, it was found that using He-containing gas mixtures for processing leads to the
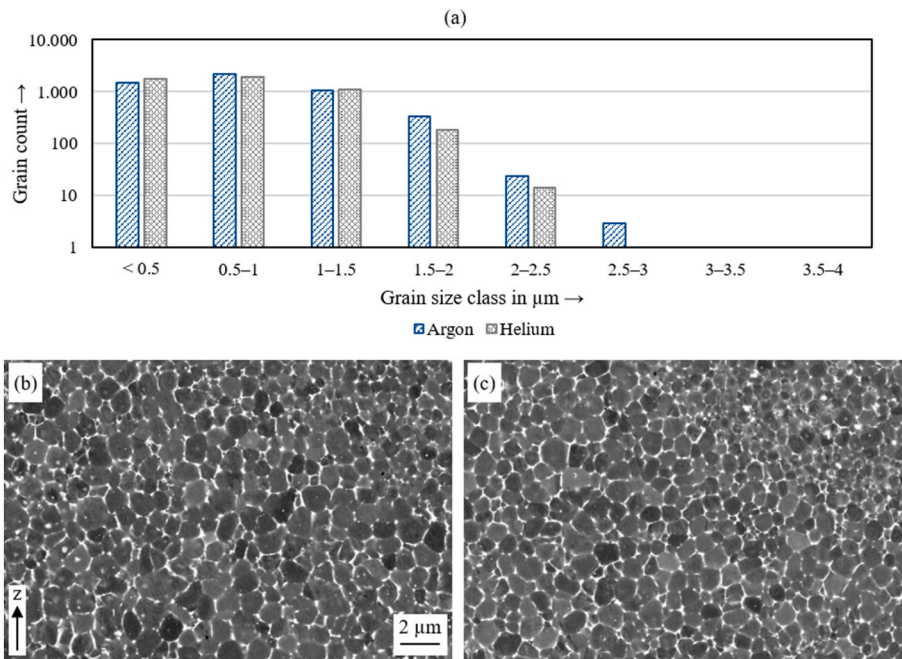
Fig. 6. (a): Logarithmic representation of the grain size analysis and distribution of the specimens processed with pure argon or helium, (b) + (c): SEM micrographs revealing the overall microstructure of the (b) argon processed and (c) helium processed samples; z: building direction.
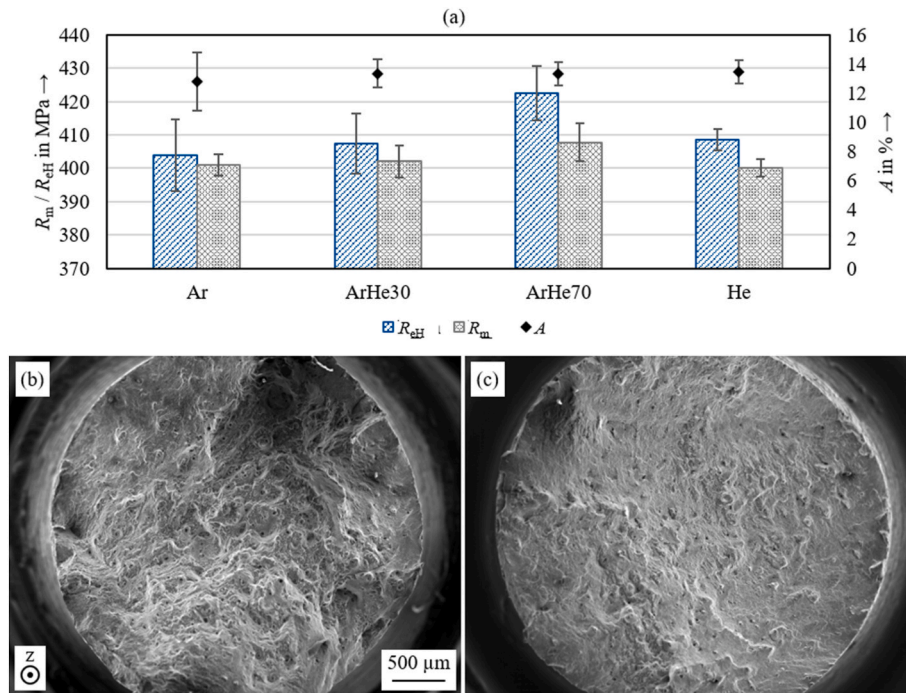

Fig. 7. (a) Results from the static mechanical tensile tests of specimens processed with various gases showing the yield strength R_{eH}, the tensile strength R_m, and the elongation at break A, (b) + (c): SEM micrographs of the fracture surfaces of the samples manufactured under (b) argon and (c) helium; z: building direction.

creation of a lower total spatter mass (Baehr et al., 2023). This could result from a more dynamically stable melt pool during He processing due to the lower recoil pressure applied by the lighter He gas. Moreover, a lower number of spatter particles potentially crosses the laser beam path when processing under He containing atmospheres leading to less localized laser attenuation and a more stable input of energy into the powder layer. This hypothesis is corroborated by the results of the porosity measurements of this study in Fig. 5, where a slightly higher overall level of densities was found in the He processed samples.

Additionally, a trend towards higher penetration depths with increasing He content in the process gas is evidence of a better energy input in the process (see Table 2). Despite some agglomerated and irregularly shaped particles in the powder bed (see Fig. 3), no deterioration of the powder spreading was observed in the processes.

4.2. Evaporation

The oxygen contents in the parts as measured by IGF (Table 3)

support the finding of a process with a relatively more stable melt pool and less spatter created under He. In Al alloys processed by PBF-LB/M, spatter particles have a net-effect of removing oxygen from the melt pool and, hence, from the bulk material since the oxygen is entrapped in the oxide layer on top of the melt pool, where spatter particles are ejected (Ghasemi et al., 2021). In the measurements, a higher oxygen content was found in the He processed samples compared to the Ar processed samples. However, any notable differences between the gases are relatively small and within the analytical uncertainty of the IGF measurements.

In terms of the evaporation of metallic elements measured by ICP-OES, no significant differences were found between the processing gases. This leads to the assumption that the differences in the higher cooling ability of He compared to Ar do not play such a major role as it is the case during spatter cooling. A reason for that could be the shorter interaction time of the gas and the melt pool compared to the gas and a spatter.

In general, differences in the degree of evaporation were found between the elements, which can be attributed to their varying boiling points and vapor pressures. The highest amount of evaporation for the volatile elements, with lower boiling points than the Al matrix, was found for Zn with a boiling temperature of 1180 K, and the lowest for Li with a boiling temperature of 1615 K (Haynes, 2014).

4.3. Microstructure and mechanical strength

The microstructure of the Al–Cu–Li–Ti alloy used in this study is consistent with those of other PBF-LB/M manufactured 2000 series Al–Cu alloys (Qi et al., 2021; Raffeis et al., 2020). There, grain refinement by the addition of Ti was found to be a functional way of mitigating cracking in high-strength Al alloys (Roscher et al., 2021). In this study, the microstructure was found to mainly consist of equiaxed grains between 0 and 4 μm (see Fig. 6). This microstructure of the as-built material is similar to that of the powder particles shown in Fig. 3 since they both form by rapid solidification in the PBF-LB/M or gas atomization process, respectively. With the use of He instead of Ar as processing gas, a shift towards smaller grains was found (see Fig. 6). This difference could be attributed to the higher cooling ability of He leading to a moderately higher cooling rate of the melt pool and, hence, finer grains. No difference in the fraction of micron scale Al_3Ti precipitates was observed between the different gases. However, the quantity and distribution of nanometric Al_3Ti precipitates was not able to be quantified. A difference in nanometric precipitate content due to the different cooling rates could be a further contributing factor along with the grain size to the mechanical properties of the material. The correlation between a higher cooling rate and a refined microstructure for an aluminum alloy is described in the literature (He et al., 2020).

The differences in the microstructure explain the varying static mechanical properties of parts being fabricated with the different gases (see Fig. 7). A higher yield and tensile strength with an increasing fraction of He in the process gas could originate from the finer grain structure of these samples. These findings match with results from the literature (Amano et al., 2021; Pauzon et al., 2022).

Investigating the fracture surfaces of the specimens processed with pure Ar or He gases led to the assumption that the He processed samples exhibit a more brittle behavior. However, considering the results for the elongation of the tensile samples, no differences were found between Ar and He processing. The differences in the fracture surfaces could rather be attributed to the different levels of porosity in the parts. For He, lower porosities were found as compared to Ar (see Fig. 5). The crack created in the He processed sample could, therefore, propagate through the part while being unhindered. In the samples fabricated under Ar, the higher density of pores might have led to increased crack deflection and more cleavage planes on the fracture surface. However, the defect density was not high enough to decrease the total elongation to fracture of the 8 mm diameter tensile coupons compared to the samples fabricated under He containing gases.

5. Conclusion

The scientific objective of this study was to unveil the influence of argon (Ar), helium (He), and their mixtures on the processing of a high-strength Al–Cu–Li–Ti alloy by the powder bed fusion of metals using a laser beam (PBF-LB/M). First, the alloy powder size, morphology, internal microstructure and chemical composition were characterized. Then, coupons were manufactured by PBF-LB/M using a full-factorial experimental plan to observe the process and to study the remaining part porosity, the penetration depth, and the microstructure. Finally, tensile bars served as test specimens for the determination of the static mechanical properties.

The main outcomes from this study on the PBF-LB/M process can be summarized as follows:

- Increasing the He content in Ar–He gas mixtures leads to
  - fewer incandescent spatters and to fewer laser-spatter interactions,
  - a more stable process with overall higher part densities and slightly higher penetration depths,
  - and smaller average grain size as well as a higher yield and tensile strength of the fabricated parts.
- No significant influence of an increasing He content in Ar–He gas mixtures was observed for the evaporation of volatile elements and for the resulting elongation of the parts.

CRediT authorship contribution statement

Siegfried Baehr: Writing – original draft, Visualization, Validation, Project administration, Methodology, Investigation, Formal analysis, Conceptualization. **Graham Matheson:** Writing – original draft, Validation, Investigation. **Thomas Ammann:** Writing – review & editing. **Peter Mayr:** Writing – review & editing, Supervision. **Michael F. Zaeh:** Writing – review & editing, Supervision, Funding acquisition.

Declaration of competing interest

The authors declare that they have no known competing financial interests or personal relationships that could have appeared to influence the work reported in this paper.

Data availability

Data will be made available on request.

Acknowledgments

Appendix A. Grinding and polishing routine (equipment and branding from Struers GmbH)

Stage	Plate	Suspension	Duration
Grinding	MD-Piano 220	Water	3 min
	MD-Largo	DiaPro Allegro/Largo	4 min
	MD-Mol	DiaPro MolB3	3 min
Polishing	MD-Chem	OP-S NonDry	1 min

Appendix B. Results from the density measurements in the samples processed under ArHe30 and ArHe70; (a) relative density, (b) absolute density
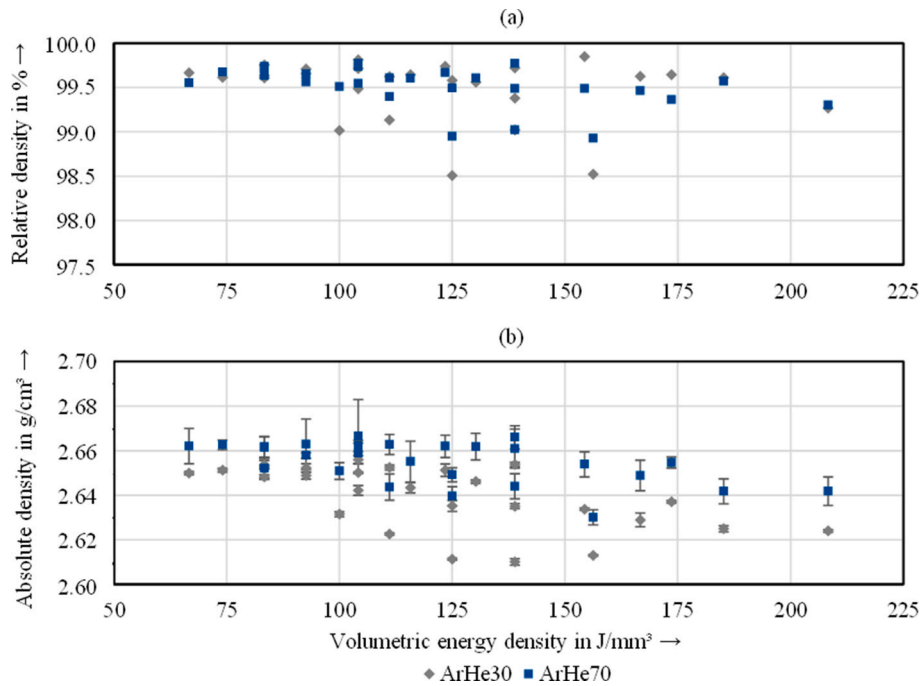

Appendix C. Summary of the ANOVA analysis for the relative density

	Degree of freedom (DF)	Sum of squares (SS)	Mean square (MS)	F value	p value
Regression	14	11.784	0.84171	14.1	0.000
Residuals	96	5.73	0.059687		
Total	110	17.5139			

	Coefficient	t value	p value		
Constant	99.4469				
Laser power P	−0.3268	−11.4934	0.000		
Scanning speed v	0.000169	0.005949	0.995		
Hatch distance h	−0.01882	−0.66178	0.510		
Gas type	0.083792	2.69699	0.008		

|	Coefficient of determination (R^2)	Adjusted coefficient of determination (R^2)			
Model summary	0.673	0.625			

Appendix D. (a): Logarithmic representation of the grain size analysis and distribution of the specimens processed with ArHe30 or ArHe70; (b) + (c): SEM micrographs corresponding to the specimens processed using gas mixtures of (b) ArHe30 and (c) ArHe70; z: building direction
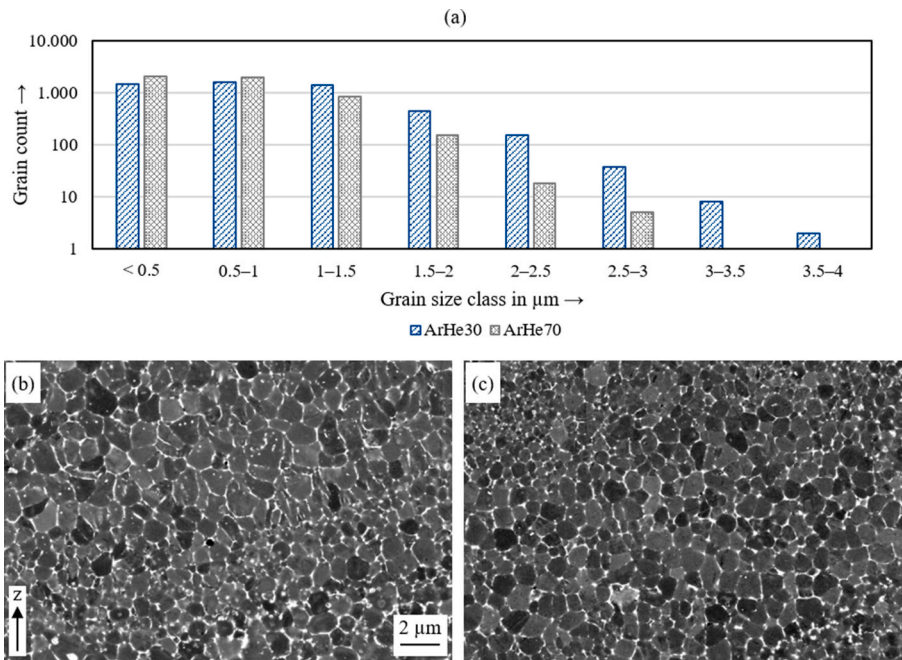
Appendix E. Displayed EBSD inverse pole figures for specimens processed with various gases; z: building direction
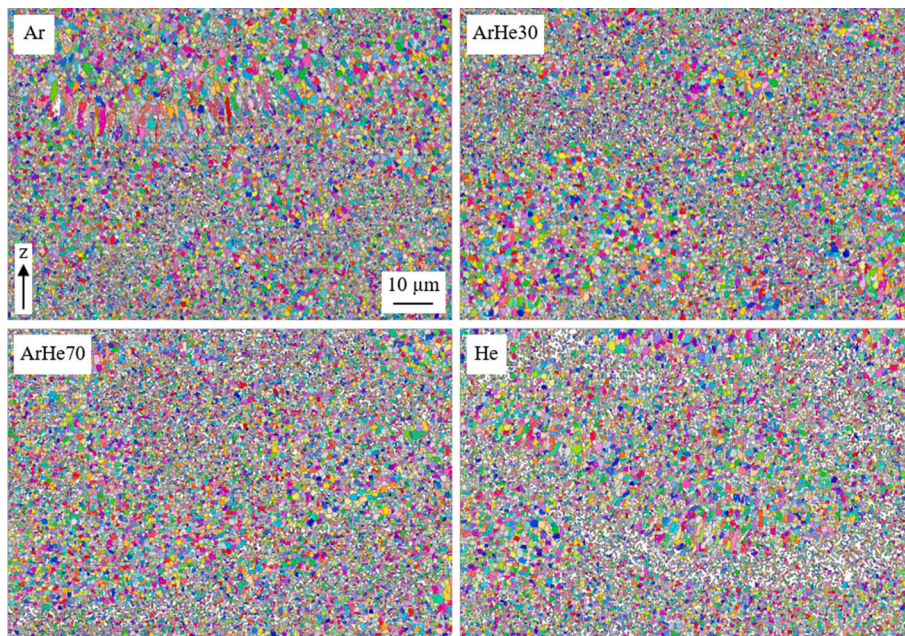
Appendix F. Fracture surfaces of the specimens processed with gas mixtures of ArHe30 and ArHe70; z: building direction
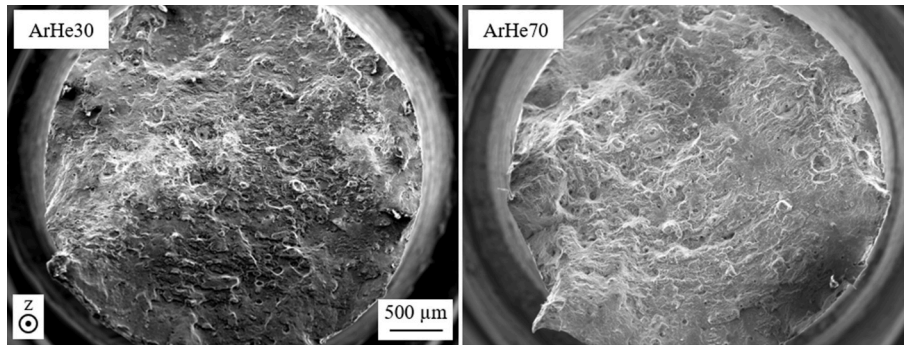
References

Amano, H., Ishimoto, T., Suganuma, R., Aiba, K., Sun, S.-H., Ozasa, R., et al., 2021. Effect of a helium gas atmosphere on the mechanical properties of Ti-6Al-4V alloy built with laser powder bed fusion: a comparative study with argon gas. Addit. Manuf. 48, 102444 https://doi.org/10.1016/j.addma.2021.102444.

Aversa, A., Marchese, G., Manfredi, D., Lorusso, M., Calignano, F., Biamino, S., et al., 2018. Laser powder bed fusion of a high strength Al-Si-Zn-Mg-Cu alloy. Metals 8 (5), 300. https://doi.org/10.3390/met8050300.

Aversa, A., Marchese, G., Saboori, A., Bassini, E., Manfredi, D., Biamino, S., et al., 2019. New aluminum alloys specifically designed for laser powder bed fusion: a review. Materials 12 (7). https://doi.org/10.3390/ma12071007.

Baehr, S., Klecker, T., Pielmeier, S., Ammann, T., Zaeh, M.F., 2023. Experimental and analytical investigations of the removal of spatters by various process gases during the powder bed fusion of metals using a laser beam. Prog. Addit. Manuf. https://doi.org/10.1007/s40964-023-00491-y.

Baehr, S., Melzig, L., Bauer, D., Ammann, T., Zaeh, M.F., 2022. Investigations of process by-products by means of Schlieren imaging during the powder bed fusion of metals using a laser beam. J. Laser Appl. 34 (4) https://doi.org/10.2351/7.0000808.

Ch, S.R., Raja, A., Nadig, P., Jayaganthan, R., Vasa, N.J., 2019. Influence of working environment and built orientation on the tensile properties of selective laser melted AlSi10Mg alloy. Mater. Sci. Eng. 750, 141–151. https://doi.org/10.1016/j.msea.2019.01.103.

Dixit, S., Liu, S., 2022. Laser additive manufacturing of high-strength aluminum alloys: challenges and strategies. J. Manuf. Mater. Process. 156 (6), 1–28. https://doi.org/10.3390/jmmp6060156.

Gebhardt, A., 2016. Additive Fertigungsverfahren: Additive Manufacturing und 3D-Drucken für Prototyping - Tooling - Produktion, fifth ed. Hanser, Munich.

Ghasemi, A., Fereiduni, E., Balbaa, M., Jadhav, S.D., Elbestawi, M., Habibi, S., 2021. Influence of alloying elements on laser powder bed fusion processability of aluminum: a new insight into the oxidation tendency. Addit. Manuf. 46 https://doi.org/10.1016/j.addma.2021.102145.

Haynes, W.M., 2014. Handbook of Chemistry and Physics. CRC Press, Taylor & Francis Group, Boca Raton, London, New York.

He, C., Yu, W., Li, Y., Wang, Z., Di, W., Xu, G., 2020. Relationship between cooling rate, microstructure evolution, and performance improvement of an Al–Cu alloy prepared using different methods. Mater. Res. Express 7 (11). https://doi.org/10.1088/2053-1591/abc4f9.

Hu, Z., Nie, X., Qi, Y., Zhang, H., Zhu, H., 2020. Cracking criterion for high strength Al–Cu alloys fabricated by selective laser melting. Addit. Manuf. 37.

Kusoglu, I.M., Gökce, B., Barcikowski, S., 2020. Research trends in laser powder bed fusion of Al alloys within the last decade. Addit. Manuf. 36 https://doi.org/10.1016/j.addma.2020.101489.

Ladewig, A., Schlick, G., Fisser, M., Schulze, V., Glatzel, U., 2016. Influence of the shielding gas flow on the removal of process by-products in the selective laser melting process. Addit. Manuf. 10, 1–9. https://doi.org/10.1016/j.addma.2016.01.004.

Mair, P., Kaserer, L., Braun, J., Weinberger, N., Letofsky-Papst, I., Leichtfried, G., 2021. Microstructure and mechanical properties of a TiB2-modified Al–Cu alloy processed by laser powder-bed fusion. Mater. Sci. Eng. 799 https://doi.org/10.1016/j.msea.2020.140209.

Mertens, R., Baert, L., Vanmeensel, K., van Hooreweder, B., 2020. Laser powder bed fusion of high strength aluminum. Mater. Des. Process. Commun. 161 (3), 1–7.

Pauzon, C., Hoppe, B., Pichler, T., Dubiez-Le Goff, S., Forêt, P., Nguyen, T., et al., 2021. Reduction of incandescent spatter with helium addition to the process gas during laser powder bed fusion of Ti-6Al-4V. CIRP J. Manuf. Sci. Technol. 35, 371–378. https://doi.org/10.1016/j.cirpj.2021.07.004.

Pauzon, C., Hryha, E., Forêt, P., Nyborg, L., 2019. Effect of argon and nitrogen atmospheres on the properties of stainless steel 316 L parts produced by laser-powder bed fusion. Mater. Des. 179, 107873 https://doi.org/10.1016/j.matdes.2019.107873.

Pauzon, C., van Petegem, S., Hryha, E., Sin Ting Chang, C., Hocine, S., van Swygenhoven, H., et al., 2022. Effect of helium as process gas on laser powder bed fusion of Ti-6Al-4V studied with operando diffraction and radiography. Eur. J. Mater. 422–435.

Qi, Y., Hu, Z., Zhang, H., Nie, X., Zhang, C., Zhu, H., 2021. High strength Al–Li alloy development for laser powder bed fusion. Addit. Manuf. 47 https://doi.org/10.1016/j.addma.2021.102249.

Raffeis, I., Adjei-Kyeremeh, F., Vroomen, U., Richter, S., Bührig-Polaczek, A., 2020. Characterising the microstructure of an additively built Al-Cu-Li alloy. Materials 13, 1–18.

Reijonen, J., Revuelta, A., Riipinen, T., Ruusuvuori, K., Puukko, P., 2020. On the effect of shielding gas flow on porosity and melt pool geometry in laser powder bed fusion additive manufacturing. Addit. Manuf. 32 https://doi.org/10.1016/j.addma.2019.101030.

Rometsch, P.A., Zhu, Y., Wu, X., Huang, A., 2022. Review of high-strength aluminium alloys for additive manufacturing by laser powder bed fusion. Mater. Des. 219, 110779 https://doi.org/10.1016/j.matdes.2022.110779.

Roscher, M., Balachandran, S., Mayweg, D., Jägle, E.A., 2021. Development of Al-Ti-based alloys for laser powder bed fusion. Addit. Manuf. 47 https://doi.org/10.1016/j.addma.2021.102315.

Schimbäck, D., Mair, P., Bärtl, M., Palm, F., Leichtfried, G., Mayer, S., et al., 2022. Alloy design strategy for microstructural-tailored scandium-modified aluminium alloys for additive manufacturing. Scripta Mater. 207, 114277 https://doi.org/10.1016/j.scriptamat.2021.114277.

Stopyra, W., Gruber, K., Smolina, I., Kurzynowski, T., Kuźnicka, B., 2020. Laser powder bed fusion of AA7075 alloy: influence of process parameters on porosity and hot cracking. Addit. Manuf. 35, 101270 https://doi.org/10.1016/j.addma.2020.101270.

Traore, S., Schneider, M., Koutiri, I., Coste, F., Fabbro, R., Charpentier, C., et al., 2021. Influence of gas atmosphere (Ar or He) on the laser powder bed fusion of a Ni-based alloy. J. Mater. Process. Technol. 288, 116851 https://doi.org/10.1016/j.jmatprotec.2020.116851.

Varmus, T., Konecna, R., Nicoletto, G., Uriati, F., 2023. Microstructure and fatigue properties of Al2024-RAM2 aluminum alloy obtained by laser powder bed fusion. Procedia Struct. Integr. 43, 184–189. https://doi.org/10.1016/j.prostr.2022.12.256.

Wimmer, A., Zeller, C., Bayerlein, F., Scherer, D., Zaeh, M.F., Forêt, P., et al., 2018. Influence of the process gas on the laser beam melting process. In: Proceedings of the 7th International Conference on Additive Technologies, pp. 66–70.

Wirth, F., Frauchiger, A., Gutknecht, K., Cloots, M., 2020. Influence of the inert gas flow on the laser powder bed fusion (LPBF) process. In: Industrializing Additive Manufacturing, AMPA, pp. 192–204.